

Trajectory Smoothing Using GNSS/PDR Integration via Factor Graph Optimization in Urban Canyons

Yihan Zhong^{ID}, Weisong Wen^{ID}, Member, IEEE, and Li-Ta Hsu^{ID}

Abstract—Smooth and accurate global navigation satellite system (GNSS) positioning for pedestrians in urban canyons is still a challenge due to the multipath effects and the nonline-of-sight (NLOS) receptions caused by the reflections from surrounding buildings. Factor graph optimization (FGO) attracts more and more attention in GNSS society for improving urban GNSS positioning by effectively exploiting the measurement redundancy from historical information to resist the outlier measurements. Unfortunately, the FGO-based GNSS standalone positioning is still challenged in highly urbanized areas. As an extension of the previous FGO-based GNSS positioning method, the potential of the pedestrian dead reckoning (PDR) model in FGO to improve the GNSS standalone positioning performance in urban canyons is exploited in this article. Specifically, the relative motion of the pedestrian is estimated based on the raw acceleration measurements from the onboard smartphone inertial measurement unit (IMU) via the PDR algorithm. Then, the raw GNSS pseudorange, Doppler measurements, and relative motion from PDR are integrated using the FGO. Given the context of pedestrian navigation with a small acceleration most of the time, a novel soft motion model is proposed to smooth the states involved in the factor graph model. This article verified the effectiveness of employing the PDR model in FGO step-by-step through two data sets collected in dense urban canyons of Hong Kong using smartphone-level GNSS receivers. The comparison between the conventional extended Kalman filter, several existing methods, and FGO-based integration is presented. The proposed method shows better results than the conventional FGO method in all test data sets, with at least a 22% decrease in the mean value of the positioning error. The proposed method reduces the average localization error from 31.64 m to 18.51 m in a deep urban area.

Index Terms—Factor graph optimization (FGO), global navigation satellite system (GNSS), navigation, nonline-of-sight (NLOS), pedestrian dead reckoning (PDR), trajectory smoothing, urban canyons.

I. INTRODUCTION

THE URBAN canyon is one of the most economic scenarios, posing a significantly increased need for accurate pedestrian navigation [1], [2]. Nowadays, Global Navigation

Manuscript received 14 December 2023; revised 15 April 2024; accepted 29 April 2024. Date of publication 3 May 2024; date of current version 9 July 2024. This work was supported in part by the Guangdong Basic and Applied Basic Research Foundation under Grant 2021A1515110771; in part by the Research Centre for Data Sciences & Artificial Intelligence, The Hong Kong Polytechnic University, through the Project “Data-driven-assisted GNSS RTK/INS Navigation for Autonomous Systems in Urban Canyons.” and in part by the supported in part by the Research Center of Deep Space Exploration, The Hong Kong Polytechnic University, through the Project “Multi-robot Collaborative Operations in Lunar Areas for Regolith Processing.” (*Corresponding author: Weisong Wen*)

The authors are with the Department of Aeronautical and Aviation Engineering, Hong Kong Polytechnic University, Hong Kong (e-mail: yi-han.zhong@connect.polyu.hk; welson.wen@polyu.edu.hk; lt.hsu@polyu.edu.hk).

Digital Object Identifier 10.1109/JIOT.2024.3396360

Satellite System (GNSS) receivers are still irreplaceable in the open area by providing reliable global positioning for users in urban environments. Unfortunately, the GNSS performs poorly in urban areas because of high-rise buildings. The obstacles would lead to the multipath effect and the nonline-of-sight (NLOS) [3]. The multipath effects and NLOS could potentially result in a significant error in GNSS positioning. Numerous researchers proposed methods to solve this problem by mitigating the impacts of the multipath effect and NLOS [4], [5], [6], [7]. Factor graph optimization (FGO)-based GNSS positioning methods [8] showed increased resistance against the potential outliers, such as the NLOS and multipath. This is achieved by exploiting measurement redundancy from multiple historical epochs using the factor graph model, where mainly two consecutive epochs of information are exploited simultaneously in the conventional extended Kalman filtering (EKF)-based method [9], [10]. A robust model was employed by the Chemnitz University of Technology team [11], [12], [13] to mitigate the outlier measurement effects in GNSS positioning using the FGO. In their work, only the raw GNSS pseudorange measurements were exploited. Recently, the FGO-based GNSS positioning developed by Dr. Suzuki [14] obtained the best accuracy in the Google smartphone challenge in ION GNSS+ 2021 [14] and ION GNSS+ 2022 [15]. His research used switchable constraints [16] together with batch optimization to maintain the trajectory smoothness. The above research showed that the FGO can mitigate the GNSS outlier’s adverse effect by using the increased measurement redundancy from historical information. However, the FGO-based GNSS standalone positioning is still challenged in deep urban canyons, resulting in 20 m of positioning error in highly urbanized areas [17].

Utilizing the inertial measurement unit (IMU) in the positioning system is one of the possible ways to assist deep urban positioning [18], [19], [20]. With the widespread adoption of the MEMS-IMU technology in smartphones, there is a growing idealization of its application as a supplement to urban navigation systems. The pedestrian dead reckoning (PDR) [21], [22], [23], [24], [25], [26] exploits the context of pedestrian navigation which can provide the relative position between two consecutive states by detecting the walking steps. Building on this foundation, Chen et al. [19] utilized electromyography signals for pedestrian navigation, significantly enhancing stride detection and distance estimation accuracy. Kang and Han [27] developed a novel system, which utilizes smartphone inertial sensors for indoor localization. Their system is distinctive for its ability to mitigate the effects of magnetic disturbances and

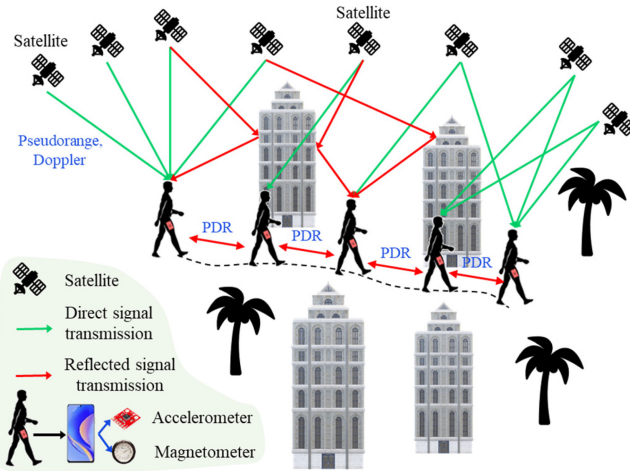


Fig. 1. Illustration of the challenges of pedestrian navigation in urban canyons with numerous GNSS signal reflections.

sensor noise, common issues in urban indoor environments. Kuang et al. [28] developed an MEMS-IMU-based robust PDR algorithm tailored for smartphones, addressing diverse carrying positions and step detection failures. Chen et al. [19], Kang and Han [27], and Cho and Park [29] proposed a novel zero-velocity detection algorithm for PDR, eliminating the dependence on predetermined thresholds and enhancing adaptability across varied walking patterns. Combining the MEMS sensor information in the mobile phone as well as the GNSS information may complement the smartphone positioning accuracy in urban areas [30], [31]. PDR demonstrates its role in urban navigation and a detailed review of PDR can be found at [32].

To enhance pedestrian navigation in urban areas, the integration of GNSS and PDR technologies has been developed [20], [33], [34], [35]. Angrisano et al. [36] enhanced urban pedestrian localization by fusing PDR with GNSS data using a loosely coupled integration architecture, showcasing improvements in scenarios with compromised GNSS signals. An integrated GNSS/PDR method to narrow the gaps in the GNSS-denied situation and utilized peak detection, slide-window, and zero crossing methods to detect pedestrian steps [33]. A real-time Kalman filter-based GNSS/PDR position method was proposed with a multirate filter to prevent GNSS information from being unavailable [20]. Some researchers utilize the EKF-based GNSS/PDR integration to improve the positioning performance of the smartphone-based navigation system in an environment that suffers the multipath effect [34]. However, these EKF-based GNSS/PDR integration fails to explore the measurement redundancy from the historical information, which inspires us to raise a new question: how would the PDR help with the existing FGO-based GNSS positioning as shown in Fig. 1? Interestingly, a work [35] investigated a loosely coupled GNSS/PDR integration using the FGO where PDR directly integrated with the position from the GNSS. Unfortunately, the loosely coupled integration in FGO could not fully exploit the strong time-correlation of the raw GNSS pseudorange measurements and the high-accuracy Doppler measurement was not exploited [10].

To effectively exploit the complementariness of the recently developed FGO-based GNSS positioning and the PDR, this article investigates a tightly coupled FGO-based GNSS/PDR integration system for smartphone-based pedestrian navigation in urban canyons. On the one hand, the relative motion estimation of PDR can help resist the potential GNSS outliers. On the other hand, the GNSS raw measurements can help to correct the accumulated drift from PDR. More importantly, the global optimization from the FGO is exploited to relax the potential of both positioning sources to obtain an accurate and smooth trajectory which is of great significance for pedestrian navigation applications. Given the context of pedestrian navigation, this article proposes a smoothness-driven motion model (SMM) that can effectively capture the dynamics of the pedestrian. The main contributions of this article are summarized as follows.

- 1) As an extension of our previous work in [17] and [37], a tightly coupled FGO-based GNSS/PDR integrated positioning method is proposed in this article. Specifically, Doppler and pseudorange measurements are tightly coupled (TC) to connect the state set of two consecutive epochs in the factor graph. The relative motion is derived from the PDR based on the raw measurements from IMU which helps to establish an additional relative connection between the consecutive states.
- 2) To effectively capture the dynamics of pedestrian navigation, this article proposes an SMM based on the context of pedestrian navigation with a small acceleration for trajectory smoothing which could also help to resist the potential GNSS outliers in GNSS standalone positioning.
- 3) In this article, the SMM and PDR factors' validity are progressively verified using a challenging data set collected in the Hong Kong urban canyon with detailed discussion. Moreover, we compare the conventional EKF-based methods with several existing methods to our proposed GNSS/PDR integration method, again showing the proposed method's effectiveness.

To the best of the author's knowledge, this work is the first to research TC GNSS pseudorange and Doppler measurements with PDR in FGO for a smoother pedestrian navigation trajectory. The remainder of this article is arranged as follows. Section II overviews the proposed GNSS/PDR integration method. Section III details the PDR model and the modeling of GNSS measurements. Section IV interprets two experimental results in urban canyons. Section V presents discussions, and finally, Section VI outlines the conclusion and future work on the proposed GNSS/PDR integration.

II. OVERVIEW OF THE PROPOSED METHOD

Our proposed FGO-based GNSS PDR positioning method is shown in Fig. 2. The input to the integrated GNSS/PDR system can be divided into two parts. The first part contains the raw pseudorange and the Doppler measurements from the GNSS receiver in the smartphone. Satellites with elevation angles (ELE) below 15 degrees or carrier-to-noise ratio (C/N0) below 20 dB-Hz will be excluded to eliminate the effect of

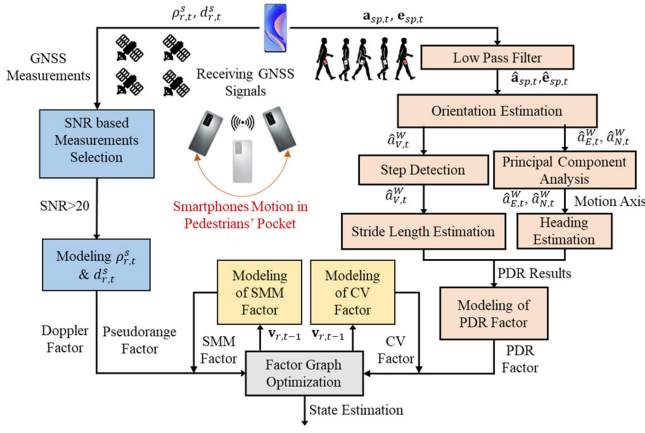


Fig. 2. Overview of the proposed FGO-based GNSS/PDR integration method.

some NLOS satellite measurements [38]. Subsequently, we compute the pseudorange and Doppler factors, essential for the estimation of the receiver's position and velocity on the global frame. PDR part [37] includes the magnetometer and accelerometer measurements. First, a low-pass filter will be employed for filtering noisy magnetometer and accelerometer measurements. Second, the filtered acceleration could be converted to the east-north-up frame with the Android API *getRotationMatrix* [39]. We use vertical acceleration for detecting steps and estimating stride length. Additionally, principal component analysis (PCA) is utilized to find the main direction of movement based on accelerations in the east and north directions. These accelerations also help in determining the user's heading. Finally, the cumulative PDR results are derived from these computations.

The proposed GNSS/PDR integration output is the smartphone's state estimation. The GNSS/PDR positioning solution can be obtained by solving the formulated factor graph which contains the TC Doppler factor, the pseudorange factor, the relative motion estimation from PDR, the SMM, and the constant velocity (CV) factor in the optimization.

To make the presentation of this article clear, the notations listed in Table I are defined and consistently used throughout. Matrices are denoted in uppercase with bold letters. Vectors are denoted in lowercase with bold letters. Variable scalars are denoted as lowercase italic letters. Constant scalars are denoted as lowercase letters. Note that, this article expresses the GNSS receiver's state, the output from PDR, and the position of satellites in the earth-centered and earth-fixed (ECEF) frame.

III. TIGHTLY COUPLED GNSS/PDR POSITIONING VIA FGO

Fig. 3 shows the factor graph of the proposed GNSS/PDR integrated positioning structure. Hollow circles denote the states to be estimated. The black circles denote the pseudorange factors and the green circles denote the Doppler frequency factors. These two factors provide the global positioning constraint in our framework. The cyan rectangular denotes the SMM factor. The PDR factor and CV factor are represented as cyan rectangular and blue rectangular, respectively. The relative motion between two consecutive

TABLE I
SYMBOLS AND THEIR DESCRIPTION IN THIS ARTICLE

Symbol	Description
r	The GNSS receiver
s	The index of the satellite
$p_{r,t}^s$	The pseudorange measurement received from a satellite s at a given epoch t .
$d_{r,t}^s$	The Doppler measurement received from satellite s at a given epoch t
\mathbf{p}_t^s	The position of the satellite s at a given epoch t . $\mathbf{p}_t^s = (p_{t,x}^s, p_{t,y}^s, p_{t,z}^s)^T$
\mathbf{v}_t^s	The velocity of the satellite s at a given epoch t . $\mathbf{v}_t^s = (v_{t,x}^s, v_{t,y}^s, v_{t,z}^s)^T$
$\mathbf{p}_{r,t}$	The position of the GNSS receiver at a given epoch t . $\mathbf{p}_{r,t} = (p_{r,t,x}, p_{r,t,y}, p_{r,t,z})^T$
$\mathbf{v}_{r,t}$	The velocity of the GNSS receiver at a given epoch t . $\mathbf{v}_{r,t} = (v_{r,t,x}, v_{r,t,y}, v_{r,t,z})^T$
$\mathbf{a}_{sp,t}$	The raw measurement from the smartphone accelerometers at a given epoch t . $\mathbf{a}_{sp,t} = (a_{sp,t,x}, a_{sp,t,y}, a_{sp,t,z})^T$
$\mathbf{e}_{sp,t}$	The raw measurement from the smartphone magnetometers at a given epoch t . $\mathbf{e}_{sp,t} = (e_{sp,t,x}, e_{sp,t,y}, e_{sp,t,z})^T$
$\hat{\mathbf{a}}_{sp,t}$	The filtered measurement from the accelerometers at a given epoch t in the global coordinate system. $\hat{\mathbf{a}}_{sp,t} = (\hat{a}_{sp,t,x}, \hat{a}_{sp,t,y}, \hat{a}_{sp,t,z})^T$
$\hat{\mathbf{e}}_{sp,t}$	The filtered measurement from the magnetometers at a given epoch t in the global coordinate system. $\hat{\mathbf{e}}_{sp,t} = (\hat{e}_{sp,t,x}, \hat{e}_{sp,t,y}, \hat{e}_{sp,t,z})^T$
$\delta_{r,t}$	The clock bias of the GNSS receiver at a given epoch t
$\delta_{r,t}^s$	The satellite clock bias at a given epoch t

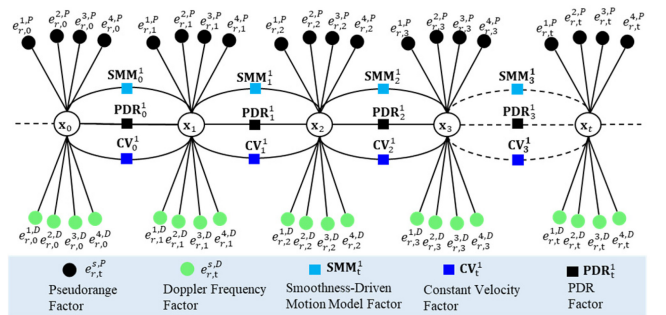


Fig. 3. Factor graph for the proposed GNSS/PDR integration.

states can be constrained by PDR, SMM, and CV factors. The smartphone-level GNSS receiver state set is represented as follows:

$$\chi = [\mathbf{x}_{r,1}, \mathbf{x}_{r,2}, \dots, \mathbf{x}_{r,t}, \dots, \mathbf{x}_{r,k}] \quad (1)$$

$$\mathbf{x}_{r,t} = (\mathbf{p}_{r,t}, \mathbf{v}_{r,t}, \delta_{r,t}, \dot{\delta}_{r,t})^T \quad (2)$$

where the variable χ denotes the state set of the smartphone-level GNSS receiver ranging from the first epoch to the current epoch k . $\mathbf{x}_{r,t}$ denotes the single state of the smartphone at epoch t which involves: 1) the position ($\mathbf{p}_{r,t}$); 2) velocity ($\mathbf{v}_{r,t}$); 3) receiver clock bias ($\delta_{r,t}$); and 4) clock drift ($\dot{\delta}_{r,t}$).

The SMM factor is created based on the assumption that the pedestrian's acceleration is close to zero, which helps in smoothing velocity changes and ultimately results in a smoother trajectory. Furthermore, by integrating the PDR

factor, the proposed method significantly enhances relative positioning accuracy.

The pseudorange and Doppler factors are utilized to estimate global position and velocity in the ECEF frame [40]. Additionally, the CV factor [41], which assumes that the pedestrian maintains a CV between two consecutive epochs, enhances relative positioning and trajectory smoothing.

A. Pseudorange Measurement Modeling

The observation model for GNSS pseudorange measurement from a given satellite s is represented as follows:

$$\rho_{r,t}^s = h_{r,t}^s(\mathbf{p}_{r,t}, \mathbf{p}_t^s, \delta_{r,t}) + \omega_{r,t}^s \quad (3)$$

with $h_{r,t}^s(\mathbf{p}_{r,t}, \mathbf{p}_t^s, \delta_{r,t}) = ||\mathbf{p}_t^s - \mathbf{p}_{r,t}|| + \delta_{r,t}$ where the variable $\omega_{r,t}^s$ stands for the noise associated with the $\rho_{r,t}^s$. We can derive the error function ($\mathbf{e}_{r,t}^{s,P}$) in proposed GNSS/PDR integration for a given satellite measurement $\rho_{r,t}^s$ as follows:

$$\|\mathbf{e}_{r,t}^{s,P}\|_{\Sigma_{r,t}^s}^2 = \|\rho_{r,t}^s - h_{r,t}^s(\mathbf{p}_{r,t}, \mathbf{p}_t^s, \delta_{r,t})\|_{\Sigma_{r,t}^s}^2 \quad (4)$$

where $\Sigma_{r,t}^s$ denotes the covariance matrix, calculated following the GO-GPS work [42] with the satellite C/N0 and ELE.

B. Doppler Measurement Modeling

The range rate measurement vector ($\mathbf{y}_{r,t}^d$) at an epoch t is expressed as follows:

$$\mathbf{y}_{r,t}^d = (\lambda d_{r,t}^1, \lambda d_{r,t}^2, \lambda d_{r,t}^3, \dots)^T. \quad (5)$$

The $d_{r,t}^s$ and λ represent the Doppler measurement and the carrier wavelength of the satellite signal, respectively. The expected range rate $rr_{r,t}^s$ for satellite s can also be calculated as follows:

$$\begin{aligned} rr_{r,t}^s &= \mathbf{e}_{r,t}^{s,\text{LOS}}(\mathbf{v}_t^s - \mathbf{v}_{r,t}) \\ &+ \frac{\omega_{\text{earth}}}{c_L} (v_{t,y}^s p_{r,t,x} + p_{t,y}^s v_{r,t,x} - p_{t,x}^s v_{r,t,y} - v_{t,x}^s p_{r,t,y}) \\ &+ \dot{\delta}_{r,t} \end{aligned} \quad (6)$$

where the variable ω_{earth} and c_L denote the angular velocity of the earth's rotation [43] and the speed of light, respectively. The variable $\mathbf{e}_{r,t}^{s,\text{LOS}}$ denotes the line-of-sight vector connecting the GNSS receiver and the satellite. Furthermore, we can derive the error function ($\mathbf{e}_{r,t}^{s,D}$) of the TC Doppler measurement as follows:

$$\|\mathbf{e}_{r,t}^{s,D}\|_{\Sigma_{r,t}^D}^2 = \|\lambda d_{r,t}^s - rr_{r,t}^s\|_{\Sigma_{r,t}^D}^2 \quad (7)$$

where $\Sigma_{r,t}^D$ denotes the covariance matrix corresponding to the Doppler measurement. And $\Sigma_{r,t}^D$ is also calculated based on the ELE and C/N0 [42]. Due to the Doppler measurements being less sensitive to the GNSS multipath effects, $\Sigma_{r,t}^D$ is multiplied by a fixed coefficient valued at 10, which means larger weightings.

C. Pedestrian Dead Reckoning Factor Modeling

1) *PDR Model*: The PDR factor is modeled by following the work in [37]. In the scenario where the pedestrian placed the smartphone in the pants pocket, the measurements of the gyroscope will be very noisy. Thus, only magnetometers and accelerometers are used in the proposed system. Both the magnetometer and accelerometer in the smartphone output 3-D measurements in local coordinates defined by the smartphone and the transformation of local coordinates to the global frame is necessary for global positioning. $\mathbf{a}_{r,t}$ and $\mathbf{e}_{r,t}$ are the accelerometer and the magnetometer measurements, respectively. Both are first used to determine the orientation of the device. The measured acceleration could be converted to the east-north-up frame with the Android API *getRotationMatrix* [39], which aims to match the tri-axis acceleration and detected gravity to get the transformation to the global coordinate. The transformed three acceleration components in the east, north, and up (ENU) frame are used to determine each step direction and step length. For attenuating the deterioration of dynamic pushes, a low-pass filtering is employed as shown below

$$\hat{\mathbf{a}}_{sp,t} = (1 - \alpha^{\text{acc}})\mathbf{a}_{sp,t} + \alpha^{\text{acc}}(\hat{\mathbf{a}}_{sp,t-1}) \quad (8)$$

$$\hat{\mathbf{e}}_{sp,t} = (1 - \alpha^{\text{mag}})\mathbf{e}_{sp,t} + \alpha^{\text{mag}}(\hat{\mathbf{e}}_{sp,t-1}) \quad (9)$$

where $\hat{\mathbf{a}}_{sp,i}$ denotes the filtered measurements of the accelerometer and $\hat{\mathbf{e}}_{sp,i}$ denotes the filtered measurements of the magnetometer. α^{acc} and α^{mag} denote the smoothing factor of the corresponding measurement field. Following the previous settings, we empirically set α^{acc} and α^{mag} as 0.6 and 0.84, respectively. The filtered measurements of acceleration can be calculated. The following part will concisely illustrate the details of the PDR method.

a) *Step Detection*: Under normal pedestrian walking conditions, the vertical acceleration $\hat{a}_{V,t}^W$ reflects a distinct peak and depression for every foot of impact. This feature makes detecting the drop in vertical acceleration as the stride rate feasible. This article empirically utilized a dip threshold at 7.5 m/s to ensure the correct detection.

b) *Stride Length Estimation*: We followed the method proposed by Weinberg [44] based on the peak-to-peak of vertical acceleration to estimate the stride length, and the model is shown as

$$l = K_w (a_{V,\max} - a_{V,\min})^{0.25} \quad (10)$$

where l denotes the estimated stride length. K_w denotes a constant for unit conversion which is empirically set as 0.713. $a_{V,\max}$ and $a_{V,\min}$ are the maximum and minimum vertical accelerations, respectively.

c) *Heading Direction Estimation*: The employed PDR method estimated the heading direction in two steps. The first step is to perform a PCA on the 2-D plane with $\hat{a}_{E,t}^W$ and $\hat{a}_{N,t}^W$, excluding the vertical direction [22]. Then, they are subjected to the covariance matrix of eigenvalue decomposition after smoothing the two sequences using a moving average. The largest eigenvalue result implies the direction estimation in the direction of parallel motion, which is the original forward direction. The second step of the heading direction estimation

is to verify whether the original forward direction derived from the PCA is correct. According to [45], vertical and forward accelerations have a time relationship in the same cycle. Usually, the forward acceleration will be followed by a peak immediately after the step detection. By using this property, the forward direction could be decided.

2) *PDR Factor*: In our approach, the PDR algorithm calculates the user's horizontal displacement within the ENU coordinate system. The initial position of the user is manually marked on Google Earth [46]. We then employ a rotation matrix $\mathbf{R}_{\text{enu}}^{\text{ref}}$ [47] to transform the PDR results from the ENU system to the ECEF coordinate system. This transformation enables us to obtain the PDR results in three dimensions within the ECEF framework. The relative displacement of the smartphone $\Delta \mathbf{p}_{\text{pdr},t}^{\text{enu}}$ could be obtained from PDR results between two consecutive frames under the ENU coordinate system

$$\Delta \mathbf{p}_{\text{pdr},t}^{\text{enu}} = [\Delta x_t^{\text{enu}}, \Delta y_t^{\text{enu}}, \Delta z_t^{\text{enu}}]^T \quad (11)$$

where Δx_t^{enu} , Δy_t^{enu} , and Δz_t^{enu} are displacement of the receiver which is obtained from the PDR in three different directions under the ENU frame. Thus, the relative displacement of the smartphone $\Delta \mathbf{p}_{\text{pdr},t}^{\text{ecef}}$ could be obtained by applying the rotation matrix $\mathbf{R}_{\text{enu}}^{\text{ecef}}$ to $\Delta \mathbf{p}_{\text{pdr},t}^{\text{enu}}$

$$\Delta \mathbf{p}_{\text{pdr},t}^{\text{ecef}} = \mathbf{R}_{\text{enu}}^{\text{ecef}} \Delta \mathbf{p}_{\text{pdr},t}^{\text{enu}}. \quad (12)$$

The difference between two consecutive epochs can be represented as

$$\Delta \mathbf{p}_{r,t} = \mathbf{p}_{r,t} - \mathbf{p}_{r,t-1} \quad (13)$$

where $\mathbf{p}_{r,t}$ denotes the position of the receiver at the t epoch and the $\mathbf{p}_{r,t-1}$ represents the position of the receiver at the $t-1$ epoch. Hence, we can get the error function ($\mathbf{e}_{r,t}^R$) for a given relative displacement $\Delta \mathbf{p}_{\text{pdr},t}^{\text{ecef}}$ as follows:

$$\|\mathbf{e}_{r,t}^R\|_{\Sigma_{r,t}^{\text{PDR}}}^2 = \|\Delta \mathbf{p}_{\text{pdr},t}^{\text{ecef}} - \Delta \mathbf{p}_{r,t}\|_{\Sigma_{r,t}^{\text{PDR}}}^2 \quad (14)$$

where $\Sigma_{r,t}^{\text{PDR}}$ denotes the covariance matrix. We set it as the fixed value for denoting the performance of the PDR factor, which is experimentally determined as 0.1.

D. Constant Velocity Factor

The CV factor is constructed based on the assumption that the speed of the pedestrian is nearly invariant in walking. In addition to the velocity remaining constant during walking, the acceleration of the receiver should also converge to zero. Hence, we can get the observation model for the smartphone-level GNSS receiver velocity ($\mathbf{v}_{r,t}$) expressed as follows:

$$\mathbf{v}_{r,t} = h_{r,t}^C(\Delta \mathbf{p}_{r,t}, \mathbf{v}_{r,t}, \mathbf{v}_{r,t+1}) + \omega_{r,t}^C \quad (15)$$

$$\text{with } h_{r,t}^C(\Delta \mathbf{p}_{r,t}, \mathbf{v}_{r,t}, \mathbf{v}_{r,t+1}) = \begin{bmatrix} \frac{\Delta p_{r,t,x}}{\Delta t} t - \frac{(v_{r,t,x} + v_{r,t+1,x})}{2} \\ \frac{\Delta p_{r,t,y}}{\Delta t} t - \frac{(v_{r,t,y} + v_{r,t+1,y})}{2} \\ \frac{\Delta p_{r,t,z}}{\Delta t} t - \frac{(v_{r,t,z} + v_{r,t+1,z})}{2} \end{bmatrix},$$

where $\mathbf{v}_{r,t}$ and $\mathbf{v}_{r,t+1}$ denote the velocity at two consecutive epochs with three dimensions in the ECEF frame, respectively.

$\Delta p_{r,t,x}$, $\Delta p_{r,t,y}$, and $\Delta p_{r,t,z}$ denote the receiver displacement between the t frame and $t+1$ frame at three dimensions. The variable $\omega_{r,t}^C$ denotes the noise associated with constant motion. Hence, the error function ($\mathbf{e}_{r,t}^C$) in our proposed GNSS/PDR integration for a given receiver velocity measurement $\mathbf{v}_{r,t}$ could be derived as follows:

$$\|\mathbf{e}_{r,t}^C\|_{\Sigma_{r,t}^C}^2 = \|h_{r,t}^C((\Delta \mathbf{p}_{r,t}, \mathbf{v}_{r,t}, \mathbf{v}_{r,t+1}))\|_{\Sigma_{r,t}^C}^2 \quad (16)$$

where $\Sigma_{r,t}^C$ denotes the covariance matrix corresponding to the receiver velocity measurement. This article empirically set $\Sigma_{r,t}^C$ as a fixed value.

E. Smoothness-Driven Motion Model Factor

Given the context of pedestrian navigation, the accelerations caused by smartphone motion tend to be small. To exploit this property which can effectively improve the smoothness of the trajectory, this article proposes an SMM factor. We can calculate the acceleration of the smartphone-level GNSS receiver $\mathbf{a}_{r,t}$ as follows:

$$\mathbf{a}_{r,t} = \begin{bmatrix} \frac{(v_{r,t+1,y} - v_{r,t,y})}{\Delta t} \\ \frac{(v_{r,t+1,y} - v_{r,t,y})}{\Delta t} \\ \frac{(v_{r,t+1,z} - v_{r,t,z})}{\Delta t} \end{bmatrix}. \quad (17)$$

Therefore, we can get the observation model for the acceleration ($\mathbf{a}_{r,t}$) expressed as follows:

$$\mathbf{a}_{r,t} = h_{r,t}^M(0, \mathbf{a}_{r,t}) + \omega_{r,t}^M \quad (18)$$

$$\text{with } h_{r,t}^M(0, \mathbf{a}_{r,t}) = \begin{bmatrix} 0 - (v_{r,t+1,y} - v_{r,t,y}) \\ \frac{0 - (v_{r,t+1,y} - v_{r,t,y})}{\Delta t} \\ \frac{0 - (v_{r,t+1,z} - v_{r,t,z})}{\Delta t} \end{bmatrix} \text{ where the variable } \omega_{r,t}^M \text{ denotes the noise associated with the zero-acceleration model. Hence, we can get the error function } (\mathbf{e}_{r,t}^M) \text{ in the proposed GNSS/PDR integration for a given receiver velocity measurement } \mathbf{v}_{r,t} \text{ as follows:}$$

$$\|\mathbf{e}_{r,t}^M\|_{\Sigma_{r,t}^M}^2 = \|\mathbf{a}_{r,t} - h_{r,t}^M(0, \mathbf{a}_{r,t})\|_{\Sigma_{r,t}^M}^2 \quad (19)$$

where $\Sigma_{r,t}^M$ denotes the covariance matrix corresponding to the receiver acceleration measurement. This article also empirically set $\Sigma_{r,t}^M$ as a fixed value. Therefore, we can formulate the objective function for the GNSS/PDR integration using the FGO based on the factors derived above as follows:

$$\chi^* = \arg \min_{\chi} \sum_{s,t} \left(\|\mathbf{e}_{r,t}^D\|_{\Sigma_{r,t}^D}^2 + \|\mathbf{e}_{r,t}^S\|_{\Sigma_{r,t}^S}^2 + \|\mathbf{e}_{r,t}^R\|_{\Sigma_{r,t}^{\text{PDR}}}^2 + \|\mathbf{e}_{r,t}^C\|_{\Sigma_{r,t}^C}^2 + \|\mathbf{e}_{r,t}^M\|_{\Sigma_{r,t}^M}^2 \right) \quad (20)$$

where the variable χ^* denotes the optimal estimation of the state sets. The Ceres Solver [48] is used as a nonlinear optimization solver for solving the objective function above. Meanwhile, the Levenberg–Marquardt (L-M) algorithm [49] is employed in our FGO processes to minimize the cost function iteratively. Additionally, we employed the Huber loss [50] to the optimizer for down-weighting some potential outliers.

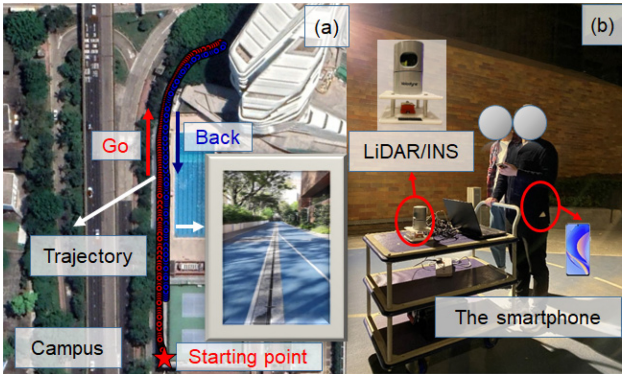


Fig. 4. Scenarios and sensor setup of the campus experiment. (a) Evaluated trajectory during the test. (b) Data collection platform with an LiDAR/INS-based ground truth system and smartphone for GNSS data collection.

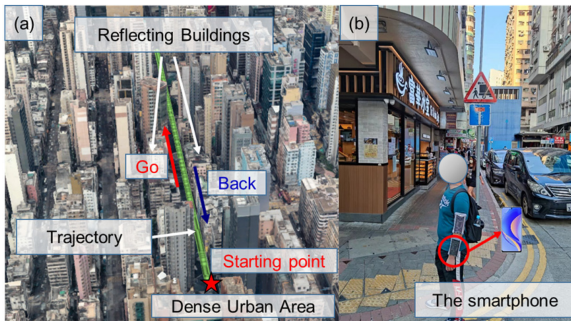


Fig. 5. Sensor setup of the dense urban area. (a) Evaluated trajectory in a dense urban canyon. (b) Data collection platform by hand-hold bag with a smartphone for GNSS data collection.

IV. EXPERIMENT RESULT AND DISCUSSION

A. Experiment Setup

We collected four data sets to verify the effectiveness of the proposed FGO-based GNSS/PDR positioning in two challenging scenarios (see Figs. 4–6), which contain many buildings or trees, resulting in many potential multipath effects and NLOS reception in the scenes. Data was gathered using a Huawei P40 Pro smartphone, collecting raw GPS and BeiDou measurements [51] at 1 Hz and IMU data at 100 Hz. The GNSS measurements were generated by the Geo++ RINEX Logger application. The GNSS hardware mode name is Hisilicon Corporation Hi1105 V100. The accelerometer and magnetometer measurements were collected via Android API [52]. The pedestrian ground truth in the first and third experiments was established using an LiDAR/inertial system comprising Velodyne HDL-32E LiDAR and Xsens Mt1 10 IMU [53]. This system utilized the LIO-SAM algorithm for SLAM, with the loop-closure constraint enhancing accuracy to submeter precision [54], [55], [56]. For the second experiment, conducted in a highly urbanized area with heavy traffic, we labeled ground truth offline using Google Earth and precise time stamps, subsequently applying linear interpolation to determine positions [46]. We used an Intel i7-9750K 2.60 GHz and a high-performance laptop with 32 GB RAM to run the proposed framework.



Fig. 6. Sensor setup of the mixed scenario. (a) Image overview with GT from Google Earth. (b) GT overview from OpenStreetMap. The LiDAR/INS system is used for generating the GT, HUAWEI P40 Pro smartphone is used for collecting the GNSS and IMU measurements. (c) Street view of the scenario from Google Earth [59].

B. Evaluation Metrics and Methods

Since the satellite geometry in dense urban canyons leads to very unreliable GNSS positioning in the vertical direction, in this article, the horizontal positioning performance will be evaluated in the ENU framework, including the root-mean-square of error (RMSE), the mean error (MEAN), standard deviation (STD), and maximum error (MAX).

To verify the effectiveness of our GNSS/PDR integration method in urban canyons step-by-step, we compared the following methods.

- 1) *FGO*: GNSS pseudorange/Doppler integration using FGO [17].
- 2) *Extended Kalman Filter With PDR (EKF-PDR)*: GNSS pseudorange/Doppler/PDR-based extended Kalman filter [57].
- 3) *FGO-CV*: CV factor aided GNSS TC Doppler/pseudorange integration using FGO [40].
- 4) *FGO-CV-SMM (1st Proposed Integration)*: The CV and SMM factors aided GNSS TC Doppler/pseudorange integration using FGO.
- 5) *FGO-PDR (2nd Proposed Integration)*: The PDR factor aided GNSS TC Doppler/pseudorange integration using FGO.
- 6) *FGO-PDR-SMM (3rd Proposed Integration)*: The PDR and SMM factors aided GNSS TC Doppler/pseudorange integration using FGO.
- 7) *FGO-PDR-CV (4th Proposed Integration)*: The PDR and CV factors aided GNSS TC Doppler/pseudorange integration using FGO.
- 8) *FGO-PDR-CV-SMM (5th Proposed Integration)*: The PDR, CV, and SMM factors aided GNSS TC Doppler/pseudorange integration using FGO.

The cost functions of these methods are listed in the Appendix in detail.

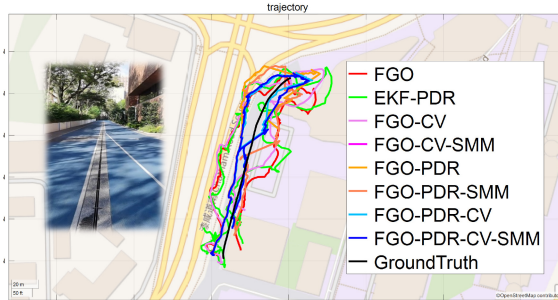


Fig. 7. Trajectories of evaluated eight methods on the campus in OpenStreetMap [60].

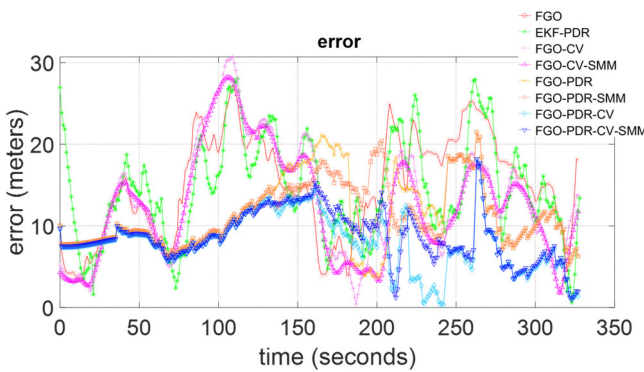


Fig. 8. Horizontal positioning errors on the campus.

The colors corresponding to each method in the subsequent trajectory and error figures are as follows.

- 1) The red denotes the FGO.
- 2) The green color denotes the EKF-PDR. The light pink and pink denote the FGO-CV and the FGO-CV-SMM, respectively.
- 3) The light orange and orange denote FGO-PDR and FGO-PDR-SMM, respectively.
- 4) The light blue and blue colors denote FGO-PDR-CV and FGO-PDR-CV-SMM, respectively.

All the FGO-based methods are post-processing methods.

The quality of the GNSS measurements will be quantified through double-difference (DD) errors. We utilized reference station data from the Hong Kong Geodetic Survey Services [58] to compute the DD pseudorange. This computation was achieved by differencing the reference station data with the receiver data. Subsequently, we combined these results with our position ground truth to ascertain the true DD range. The true DD range was determined by resolving the satellite positions using the ground truth of the reference station. The discrepancy between the DD range and the DD pseudorange was then used to define the error in the DD pseudorange. The detailed derivation is in the Appendix.

C. Experimental Evaluation on Campus

The 2-D positioning trajectories in OpenStreetMap [60] and horizontal errors of all the listed positioning methods on the campus are shown in Figs. 7 and 8. From Fig. 7, the trajectory of FGO-PDR-CV-SMM (blue curve) is consistent with the characteristics of pedestrian movement after applying

TABLE II
POSITIONING PERFORMANCE OF THE LISTED METHODS
IN THE CAMPUS EXPERIMENT

All Methods	RMSE (m)	MEAN (m)	STD (m)	MAX (m)
FGO	16.17	14.97	6.13	27.23
EKF-PDR	15.80	14.57	6.13	28.05
FGO-CV	14.85	13.13	6.94	30.69
FGO-CV-SMM	14.17	12.53	6.64	28.22
FGO-PDR	12.17	11.32	4.46	21.47
FGO-PDR-SMM	11.99	11.41	3.69	21.48
FGO-PDR-CV	8.63	7.97	3.33	17.98
FGO-PDR-CV-SMM	9.24	8.71	3.07	18.19

TABLE III
HORIZONTAL POSITIONING IMPROVEMENTS OF THE LISTED
METHODS IN THE CAMPUS EXPERIMENT

Improvements	RMSE (m)	MEAN (m)	STD (m)	MAX (m)
FGO	/	/	/	/
EKF-PDR	2.27%	2.65%	0.07%	-3.02%
FGO-CV	8.19%	12.26%	-13.10%	-12.74%
FGO-CV-SMM	12.36%	16.29%	-8.19%	-3.65%
FGO-PDR	24.77%	24.35%	27.31%	21.16%
FGO-PDR-SMM	25.86%	23.77%	39.82%	21.10%
FGO-PDR-CV	46.61%	46.77%	45.69%	33.95%
FGO-PDR-CV-SMM	42.88%	41.78%	49.94%	33.19%

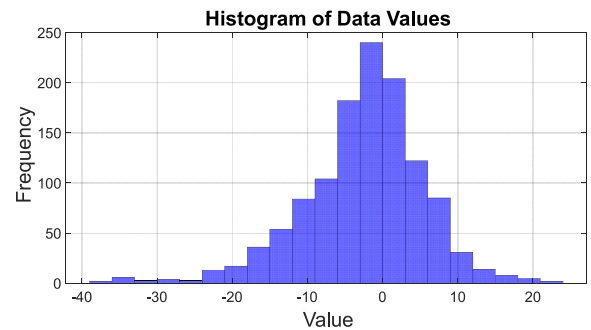


Fig. 9. Histogram of the DD pseudorange error in campus experiment.

the PDR factor, CV factor, and SMM factor. Fig. 8 shows that adding the PDR factor could significantly reduce the positioning error around 50 and 150 epochs. Detailed statistic analyses of horizontal errors are shown in Tables II and III.

The histogram of DD pseudorange errors in the campus experiment is shown in Fig. 9. The distribution of errors ranges from about -40 to 20 m shows that there are errors in the pseudorange of this data that would lead to the degraded positioning performance.

FGO can achieve 14.97 m of mean error with 6.13 m STD. However, judging from the fact that the maximum error of FGO still reaches 27.23 m, the impact of unhealthy GNSS measurements on FGO is fatal. Applying the TC Doppler factor with the CV factor (FGO-CV) could decrease the mean error to 13.13 m. This phenomenon shows that the CV factor with TC Doppler can effectively improve positioning performance. However, the CV factor based on pedestrian motion law lacks constraints on acceleration for resisting potential GNSS outliers which would lead to an unsMOOTH trajectory in GNSS-standalone positioning. After applying our proposed SMM factor, the mean error decreases to 12.53 m

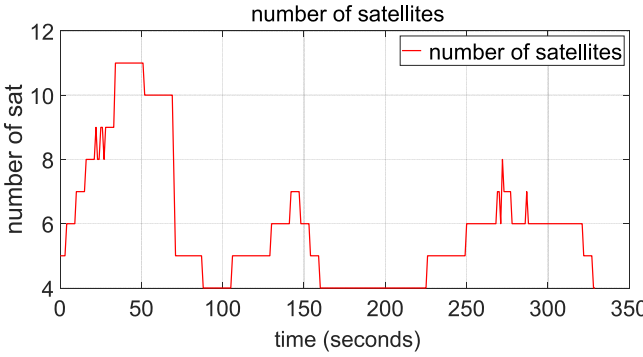


Fig. 10. Relationship between the number of satellites with time in the campus experiment.

which outperforms FGO-CV. However, the insufficiency in satellite numbers and unhealthy GNSS multipath effects would lead to limited improvement. The mean error can achieve 11.32 m with an STD of 4.46 m after applying the PDR to the TC Doppler FGO (FGO-PDR) instead of the CV factor. This improvement compared with the FGO-CV shows that the PDR factor could provide better relative position constraint between two consecutive epochs. Adding the SMM factor to the FGO-PDR could achieve a lower mean of error. However, the improvement is still limited because the PDR factor contains the error source from the smartphone accelerometer and magnetometer which may not obey the pedestrian motion law. The effectiveness of the proposed CV factor could be verified with a 7.97 m mean error of the FGO-PDR-CV, which adds the CV factor. Interestingly, the STD of error could achieve 3.07 m after applying the SMM factor in FGO-CV-PDR-SMM, but with a larger mean of errors than the FGO-CV-PDR. This is due to the occasional nonzero acceleration of the pedestrian during walking in this scenario.

GNSS/PDR method based on EKF was also evaluated. Its RMSE is 15.80 m, slightly higher than the FGO-CV and FGO-CV-SMM. This phenomenon indicates that our tightly couple GNSS standalone FGO outperforms the EKF-PDR. The number of satellites in the campus experiment over time is shown in Fig. 10. The number of satellites fluctuates during 75 to 150 epochs, which is not ideal for GNSS positioning. We can also see that the errors of the FGO-PDR (light orange curve) are significantly smaller than the errors of the FGO (red curve) and FGO-CV-SMM (pink curve) during this time which proves that our proposed PDR factor can still play a role in maintaining the need for pedestrian navigation in the GNSS denied environment.

D. Experimental Evaluation in a Dense Urban Area

To challenge the effectiveness of the SMM factor and PDR factor for localization in complex scenes, we conducted another experiment in an even denser urban area. Fig. 11 shows the pseudorange quality of this data set in terms of the DD pseudorange error. The max error is larger than 200 m, and the mean value of the DD pseudorange error is 30.55 m. The STD value is 43.739.

Tables IV and V show the above FGO-based GNSS/PDR integration methods positioning performances. The mean error

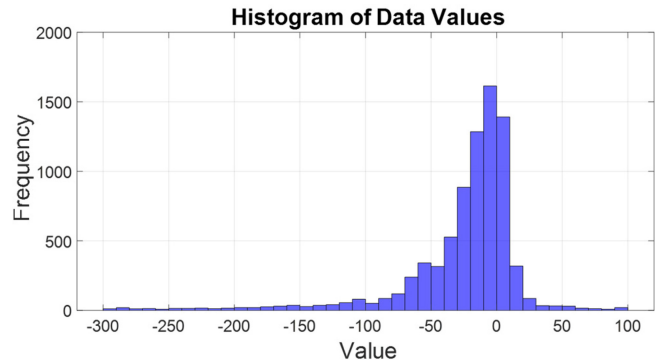


Fig. 11. Histogram of the DD pseudorange error in the dense urban experiment.

TABLE IV
POSITIONING PERFORMANCE OF THE LISTED
METHODS IN DENSE URBAN CANYON

All Methods	RMSE (m)	MEAN (m)	STD (m)	MAX (m)
FGO	19.61	16.80	10.11	76.29
EKF-PDR	26.20	21.39	15.15	148.74
FGO-CV	20.53	17.50	10.74	108.94
FGO-CV-SMM	19.42	16.66	9.97	74.02
FGO-PDR	15.12	13.55	6.72	56.92
FGO-PDR-SMM	15.12	13.55	6.72	57.00
FGO-PDR-CV	14.51	13.20	6.04	50.01
FGO-PDR-CV-SMM	14.36	13.10	5.88	45.09

TABLE V
IMPROVEMENTS OF THE LISTED METHODS IN DENSE URBAN CANYON

Improvements	RMSE (m)	MEAN (m)	STD (m)	MAX (m)
FGO	/	/	/	/
EKF-PDR	-33.64%	-27.28%	-49.83%	-94.95%
FGO-CV	-4.72%	-4.16%	-6.25%	-42.80%
FGO-CV-SMM	0.96%	0.82%	1.33%	2.98%
FGO-PDR	22.87%	19.35%	33.55%	25.39%
FGO-PDR-SMM	22.87%	19.37%	33.52%	25.29%
FGO-PDR-CV	25.98%	21.46%	40.22%	34.45%
FGO-PDR-CV-SMM	26.78%	22.05%	41.84%	40.91%

of FGO is 16.80 in this scenario, which is larger than the one in the campus experiment (14.97 m) due to the denser buildings which are more adverse for satellite signal transmission. After applying the SMM factor, the FGO-CV-SMM could outperform FGO. This phenomenon confirms that our proposed SMM factor can effectively resist GNSS outliers in dense urban areas. Interestingly, FGO-PDR and FGO-PDR-SMM show similar performance. FGO-PDR-CV decreased the error to 13.20 m, which verified the effectiveness of the assumption of CV in pedestrian navigation. After applying the SMM factor (FGO-PDR-CV-SMM), the mean error can decrease to 13.10 m, which confirms the SMM factor's effectiveness in resisting potential GNSS outliers in GNSS/PDR integrating positioning in this scenario.

Figs. 12 and 13 show the 2-D positioning trajectory in OpenStreetMap [60] and horizontal positioning errors in the dense urban scenario. In this scenario, the ground truth is a straight line, so we can easily compare the smoothness of all the methods. It is found that the GNSS pseudorange degrades

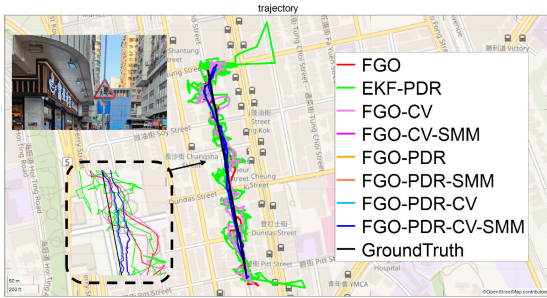


Fig. 12. Trajectories of evaluated eight methods in the dense urban canyon in OpenStreetMap [60].

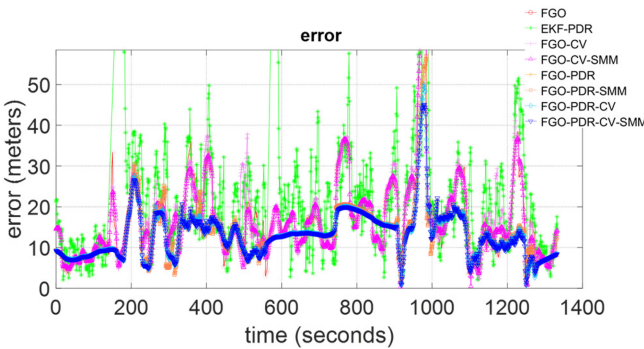


Fig. 13. Horizontal positioning errors in the dense urban experiment.

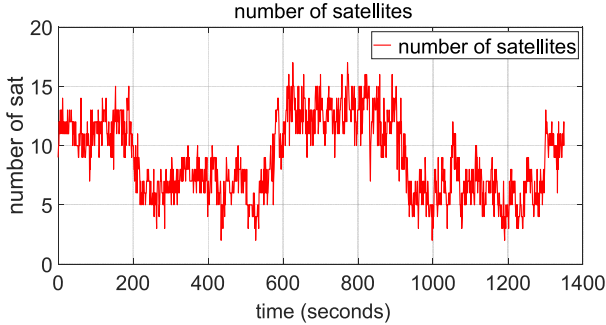


Fig. 14. Relationship between the number of satellites with time in the dense urban experiment.

due to signal reflections in dense urban environments would result in outliers that are terrible for the EKF-PDR (green curve). EKF-PDR results are worse than the GNSS-standalone FGO in this scenario, which shows a large error compared to the ground truth. Compared to FGO, FGO-PDR-CV-SMM shows a smoother trajectory.

Fig. 14 shows the number of satellites in the deep urban experiment with time. FGO-CV (light pink) and FGO-CV-SMM (pink curve), which without adding the PDR factor, reach an error close to 30 m during epoch 250–400. The FGO-PDR (light orange curve) with the PDR factor added also shows resistance to the decreased data redundancy caused by the insufficient number of satellites.

E. Experimental Evaluation in the Mixed Scenario

For a more comprehensive evaluation of the proposed method, we conducted one additional experiment. Fig. 15

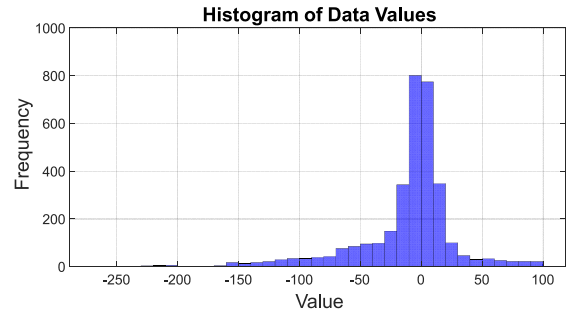


Fig. 15. Histogram of the DD pseudorange error in mixed scenario.

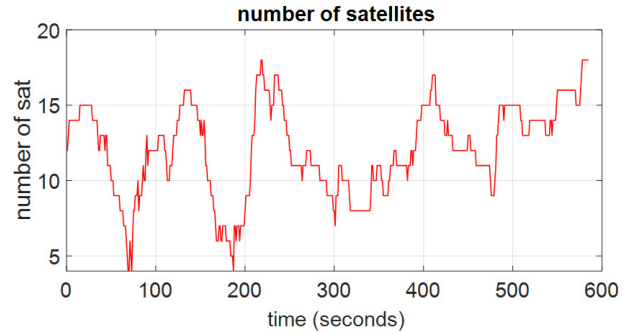


Fig. 16. Relationship between the number of satellites with time in the mixed scenario experiment.

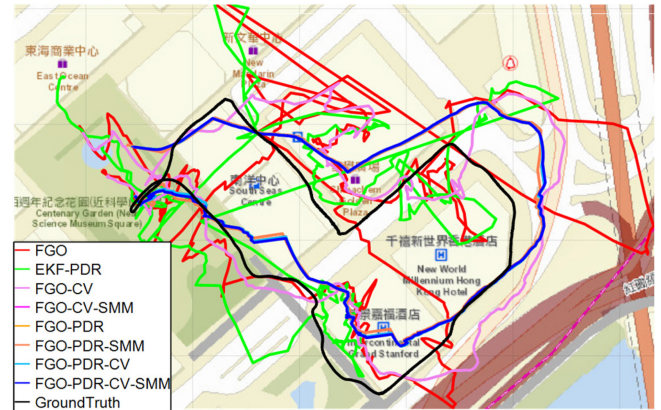


Fig. 17. Trajectories of evaluated eight methods in the mixed scenario in OpenStreetMap [60].

shows the DD pseudorange error distribution of this mixed scenario data set. The mean value of the DD pseudorange error is 24.93 m and the STD value of the errors is 33.90. Fig. 16 shows satellite numbers at each epoch in this experiment. In most cases, the number of satellites is around ten. In extreme cases, there are only four satellites. Fig. 17 shows the paths of eight different localization methods in the mixed scenario. The original FGO method performs very poorly in the mixed scene, which is due to the multipath effect present in the scene and the NLOS reception, and there is no motion model in the method, the motion constraints between frames are provided by the Doppler velocity factor [17]. Similar conclusions can be derived from Fig. 18 which shows the 2-D positioning errors of all the methods. Table VI shows the statistical results of all the methods. The baseline algorithm, FGO, exhibited initial

TABLE VI
POSITIONING PERFORMANCE OF THE LISTED
METHODS IN THE MIXED SCENARIO

All Methods	RMSE (m)	MEAN (m)	STD (m)	MAX (m)
FGO	39.23	31.64	23.21	149.16
EKF-PDR	35.20	29.58	19.10	144.03
FGO-CV	26.00	22.85	12.42	63.43
FGO-CV-SMM	25.60	22.29	12.59	57.91
FGO-PDR	21.23	18.57	10.31	36.53
FGO-PDR-SMM	21.66	18.84	10.70	39.88
FGO-PDR-CV	21.23	18.57	10.31	36.53
FGO-PDR-CV-SMM	21.20	18.51	10.34	36.41

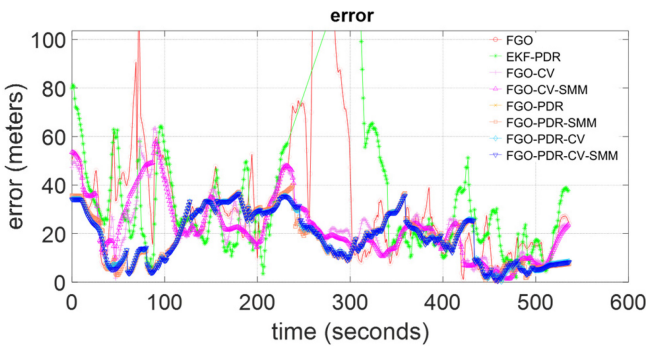


Fig. 18. Horizontal positioning errors in the mixed scenario with time.

values of 39.23 m RMSE, 31.64 m mean, 23.21 m STD, and a maximum error of 149.16 m.

Upon integrating the EKF-PDR, we observed an overall performance increase with reductions in all metrics: the RMSE decreased to 35.20 m, mean to 29.58 m, STD to 19.10 m, and max to 144.03 m. This indicates an enhanced accuracy in the EKF-PDR algorithm over the standalone FGO which shows the improvement from PDR. The FGO-CV variant showed a significant improvement, particularly in the Maximum error, which was reduced to 63.43 m, suggesting that the CV factor greatly contributes to limiting the maximum deviation of the algorithm under pedestrian walking conditions. The RMSE also has a notable reduction to 26.00 m. Further incremental improvements were observed with the addition of the SMM factor in the FGO-CV-SMM configuration, with a slight decrease in the mean error to 22.29 m and an increase in STD to 12.59 m, indicating a slightly increased variability in the errors. Substantial improvements were achieved by the FGO-PDR, which reduced the RMSE to 21.23 m and the max error to a remarkable 36.53 m. This is indicative of significant enhancements in algorithm precision and reliability. Including the SMM factor to form the FGO-PDR-SMM configuration resulted in a minimal increase in STD and max, suggesting that the SMM factor may introduce some variability under certain experimental conditions. The consistency of the performance was observed in the FGO-PDR-CV and FGO-PDR-CV-SMM configurations, which maintained the RMSE around 21.20 m, and the max error around 36.41 m. These configurations represent the most balanced approach, with improvements across all metrics. With adding the SMM factor, the mean and RMSE are slightly decreasing to 18.51 and 21.20 m,

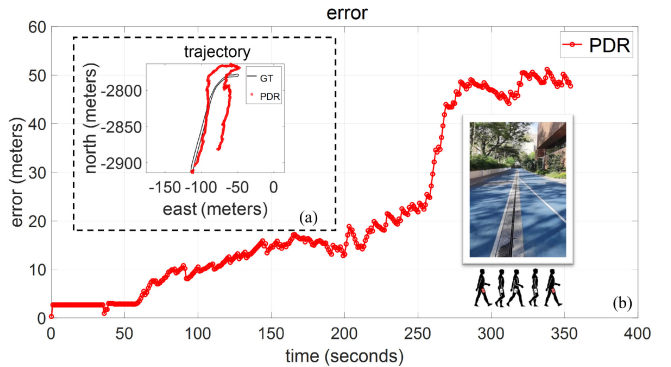


Fig. 19. (a) Horizontal PDR positioning trajectory in the campus experiment. The GT is the black curve. PDR trajectory is represented as the red curve. (b) 2-D positioning error of the PDR in the campus experiment. The red curve denotes the PDR error.

TABLE VII
PERFORMANCE OF THE PDR IN CAMPUS EXPERIMENT

Items	RMSE (m)	MEAN (m)	STD (m)	MAX (m)
PDR	26.74	21.04	16.52	51.18

respectively. In conclusion, the integration of PDR, CV, and SMM components has proven to be highly effective in refining the accuracy and consistency of the algorithm. The experimental results indicate that these configurations can significantly enhance performance in complex urban environments, yielding a reliable algorithm that consistently minimizes errors.

V. DISCUSSION

A. Discussion on PDR Results

Table VII shows the performance of the employed PDR in the campus experiment. Fig. 19 shows the employed PDR algorithm's horizontal trajectory and error. The PDR algorithm accumulated the errors over time, resulting in a very significant error in the PDR positioning results compared to the ground truth from the trajectory. The mean value of the positioning error of the PDR localization algorithm in the campus experiment is 21.04 m, while the RMSE is 26.74 m.

Fig. 20 shows the error between 70–140 s in the campus experiment. During this period, the PDR algorithm has lower errors than the FGO-CV-SMM, indicating that the proposed PDR factor provides better constraints than the CV factor in the estimation process.

B. Discussion on the Open-Sky Scenario

Fig. 21 shows the configuration of the seaside experiment. In this scenario, we use U-Blox Zed-F9P to collect GNSS L1/L2 signals in 1 Hz. The GT of this area is generated by the RTKLIB [43]. We use the combined mode real-time kinematic (RTK) for calculating the GT by manually checking the positions and trajectories. Fig. 22 shows the horizontal positioning errors of the eight methods in this open-sky area.

Table VIII shows the statistical results of the eight methods in this area. After incorporating the PDR factor into the system, the FGO-PDR-CV has shown decreasing performance

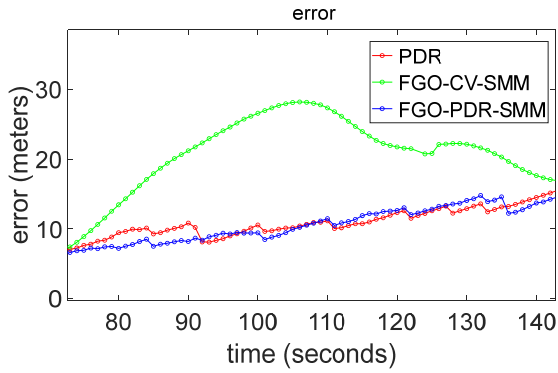


Fig. 20. 2-D positioning error of PDR, FGO-CV-SMM, and FGO-PDR-SMM between 70 to 140 epochs in the campus experiment. The red, green, and cyan curves denote PDR, FGO-CV-SMM, and FGO-PDR-SMM, respectively.

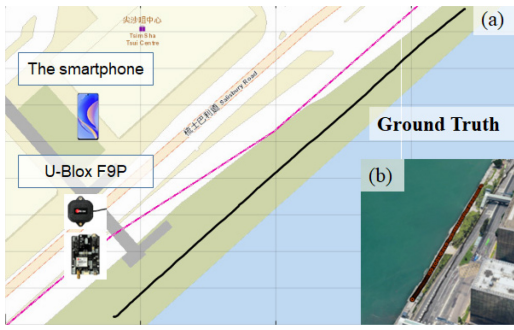


Fig. 21. Sensor setup of the seaside data set. (a) Image overview with GT from Google Earth. (b) GT overview from OpenStreetMap. U-Blox F9P system is used for generating the GT with RTK. The HUAWEI P40 Pro smartphone is used for collecting the GNSS and IMU measurements.

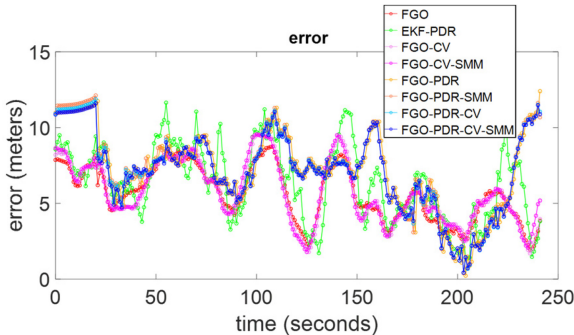


Fig. 22. Horizontal positioning errors in the seaside experiment.

compared to the FGO-CV. These results show that the PDR would introduce the errors from the noisy smartphone IMU. Original FGO shows the best performance which is better than FGO-CV. It might indicate that in this scenario, doppler velocity would provide better constraints for the two consecutive states.

C. Discussion on GNSS Measurements Residuals

The performance improvement of the FGO-PDR compared to FGO-CV-SMM demonstrates the effectiveness of the PDR factor. Regarding the two pipelines, the investigation of the residuals after the convergence from the GNSS measurement

TABLE VIII
POSITIONING PERFORMANCE OF THE LISTED METHODS
IN THE SEASIDE SCENARIO

All Methods	RMSE (m)	MEAN (m)	STD (m)	MAX (m)
FGO	5.89	5.62	1.79	8.73
EKF-PDR	6.85	6.38	2.51	11.65
FGO-CV	6.08	5.74	2.02	9.56
FGO-CV-SMM	6.09	5.76	2.00	9.56
FGO-PDR	7.66	7.21	2.61	12.40
FGO-PDR-SMM	7.69	7.22	2.65	12.12
FGO-PDR-CV	7.61	7.15	2.59	11.87
FGO-PDR-CV-SMM	7.55	7.11	2.55	11.61

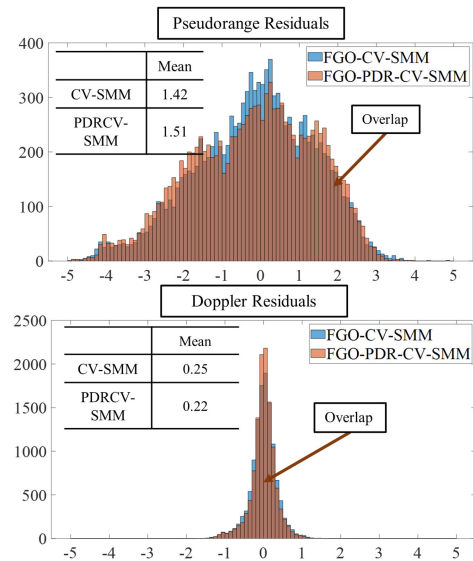


Fig. 23. Histograms of pseudorange factor and Doppler factor residuals. The x-axis denotes the value of residuals. The y-axis denotes the counts of residuals within the histogram.

models provides insights into the impact of the PDR factor on the derived solution. Ideally, the smaller residuals of applied measurements should potentially lead to more accurate estimation results, as a more consistent solution is derived given the assumption that the percentage of the healthy measurements exceeds the one from the polluted measurements. Fig. 23 shows the histogram comparison of pseudorange and Doppler factor residuals after the optimization using the listed two methods. For the pseudorange measurement, it is shown that the peak of the FGO-CV-SMM pseudorange factor residuals around 0 is higher than the one from the FGO-PDR-CV-SMM. It is well-known that pseudorange is essential for the GNSS standalone positioning because it would offer the absolute position solution. The positioning results of FGO-PDR-CV-SMM can still perform better with larger pseudorange residuals, compared with the FGO-CV-SMM.

Interestingly, a different phenomenon occurs in Doppler residuals. The mean value of the FGO-CV-SMM Doppler factor residuals is higher than the mean value of the FGO-PDR-CV-SMM residuals. The potential reason is that the

Doppler is less affected by the multipath effect while the pedestrian is walking along the street [61]. As a result, the assumption that the percentage of healthy measurements exceeds the one from polluted measurements could be largely held for the Doppler measurements.

VI. CONCLUSION AND FUTURE WORK

Pedestrian navigation in urban canyons remains a challenging task. We propose an FGO-based GNSS/PDR positioning method in this article, which tightly combines the GNSS raw measurements and the PDR outputs for accurate pedestrian positioning and smoother trajectory estimation. We also verify the effectiveness of the assumption that pedestrians have small acceleration for trajectory smoothing. Applying the SMM factor could help resist the potential GNSS outliers.

We will employ carrier-phase measurements in our GNSS/PDR integration method in the future, providing more accurate positioning performance. We will also work on real-time sliding window-based FGO GNSS/PDR positioning to reduce the computational load for smartphone-level devices by adopting the marginalization strategy [62]. We will also exploit collaborative positioning, which could improve measurement redundancy for better positioning performance in the future.

APPENDIX

A. Details of the Evaluated Methods

1) *FGO*: This is the baseline of the evaluation [17]. It utilized the GNSS pseudorange measurements and the Doppler velocity of the receiver calculated by least square. Different from the proposed method in this article, it does not TC the Doppler measurements and only considers the factors constructed by the GNSS raw measurements in the system. The cost function of this system is

$$\chi^* = \sum_{s,t} \left(\|\mathbf{e}_{r,t}^D\|_{\Sigma_{r,t}^D}^2 + \|\mathbf{e}_{r,t}^s\|_{\Sigma_{r,t}^s}^2 \right) \quad (21)$$

where $\mathbf{e}_{r,t}^D$ is the Doppler velocity factor, which is used to provide the constraints between the consecutive epochs for GNSS receivers. The pseudorange factor estimates the GNSS receiver's global position, while the Doppler velocity constrains its relative motion.

2) *EKF-PDR*: This system follows our previous research [57]. We employed the same method to estimate the receiver state as our previous loosely coupled GNSS-INS integration using the EKF. The PDR provides the translation between two epochs. In detail, the generic dynamic model of the EKF-PDR can be written as

$$\mathbf{x}_k = f(\mathbf{x}_{k-1}, \mathbf{u}_k) + \mathbf{w}_k \quad (22)$$

where \mathbf{x}_k denotes the state-space of the system. $f(\mathbf{x}_{k-1}, \mathbf{u}_k)$ denotes the state transition function which can be written as

$$f(\mathbf{x}_{k-1}, \mathbf{u}_k) = \begin{bmatrix} x_{k-1,r}^{ecef} + \Delta x_{k-1}^{ecef} \\ y_{k-1,r}^{ecef} + \Delta y_{k-1}^{ecef} \\ z_{k-1,r}^{ecef} + \Delta z_{k-1}^{ecef} \end{bmatrix} \quad (23)$$

where Δx_t^{ecef} , Δy_t^{ecef} , and Δz_t^{ecef} are displacement of the receiver which is obtained from the PDR in three different directions (ECEF frame). $x_{k-1,r}^{ecef}$, $y_{k-1,r}^{ecef}$, and $z_{k-1,r}^{ecef}$ are the receiver position at the $k-1$ epoch in three different directions (ECEF frame).

3) *FGO-CV* [40]: CV factor aided GNSS TC Doppler/pseudorange integration using FGO. The cost function of this graph can be written as

$$\chi^* = \sum_{s,t} \left(\|\mathbf{e}_{r,t}^D\|_{\Sigma_{r,t}^D}^2 + \|\mathbf{e}_{r,t}^s\|_{\Sigma_{r,t}^s}^2 + \|\mathbf{e}_{r,t}^C\|_{\Sigma_{r,t}^C}^2 \right) \quad (24)$$

where $\|\mathbf{e}_{r,t}^D\|_{\Sigma_{r,t}^D}^2$ represents the TC Doppler frequency factor, detailed in Section III. The covariance $\Sigma_{r,t}^D$ is calculated using the satellite's C/N0 and ELE. Similarly, $\|\mathbf{e}_{r,t}^s\|$ is the pseudorange factor, also explained in Section III, with its covariance $\Sigma_{r,t}^s$ derived from the satellite C/N0 and the ELE. The CV factor, denoted by $\|\mathbf{e}_{r,t}^C\|_{\Sigma_{r,t}^C}^2$, is used for smoothing the trajectory, where $\Sigma_{r,t}^C$ is empirically set as a fixed value.

4) *FGO-CV-SMM* (1st Proposed Integration): The CV and SMM factors aided GNSS TC Doppler/pseudorange integration using FGO. The cost function can be written as

$$\chi^* = \arg \min_{\chi} \sum_{s,t} \left(\|\mathbf{e}_{r,t}^D\|_{\Sigma_{r,t}^D}^2 + \|\mathbf{e}_{r,t}^s\|_{\Sigma_{r,t}^s}^2 + \|\mathbf{e}_{r,t}^C\|_{\Sigma_{r,t}^C}^2 + \|\mathbf{e}_{r,t}^M\|_{\Sigma_{r,t}^M}^2 \right). \quad (25)$$

This method employs the FGO with FGO-CV. It incorporates the SMM factor, denoted by $\|\mathbf{e}_{r,t}^M\|_{\Sigma_{r,t}^M}^2$. The covariance $\Sigma_{r,t}^M$ is empirically set as a fixed value in this factor.

5) *FGO-PDR* (2nd Proposed Integration): The PDR factor aided GNSS TC Doppler/pseudorange integration using FGO. The error function of this method can be written as

$$\chi^* = \arg \min_{\chi} \sum_{s,t} \left(\|\mathbf{e}_{r,t}^D\|_{\Sigma_{r,t}^D}^2 + \|\mathbf{e}_{r,t}^s\|_{\Sigma_{r,t}^s}^2 + \|\mathbf{e}_{r,t}^R\|_{\Sigma_{r,t}^PDR}^2 \right). \quad (26)$$

This method represents a revised version of the FGO-CV approach. In this adaptation, the CV factor is substituted with the PDR factor, which integrates PDR results to constrain the relative motion within our framework. $\|\mathbf{e}_{r,t}^R\|_{\Sigma_{r,t}^PDR}^2$ denotes the PDR factor and the covariance $\Sigma_{r,t}^PDR$ in this factor is empirically set as the fixed value.

6) *FGO-PDR-SMM* (3rd Proposed Integration): The PDR and SMM factors aided GNSS TC Doppler/pseudorange integration using FGO. The error function of this graph can be written as

$$\chi^* = \arg \min_{\chi} \sum_{s,t} \left(\|\mathbf{e}_{r,t}^D\|_{\Sigma_{r,t}^D}^2 + \|\mathbf{e}_{r,t}^s\|_{\Sigma_{r,t}^s}^2 + \|\mathbf{e}_{r,t}^R\|_{\Sigma_{r,t}^PDR}^2 + \|\mathbf{e}_{r,t}^M\|_{\Sigma_{r,t}^M}^2 \right). \quad (27)$$

FGO-PDR-SMM is a revised version of FGO-PDR with adding the SMM factor for smoothing the trajectory of FGO-PDR. Where $\|\mathbf{e}_{r,t}^D\|_{\Sigma_{r,t}^D}^2$ represents the TC Doppler frequency factor, detailed in Section III. The covariance $\Sigma_{r,t}^D$ is calculated

using the satellite's C/N0 and ELE. Similarly, $\|\mathbf{e}_{r,t}^s\|$ is the pseudorange factor, also explained in Section III, with its covariance $\Sigma_{r,t}^s$ derived from the satellite C/N0 and ELE. $\|\mathbf{e}_{r,t}^R\|_{\sum_{r,t}^{\text{PDR}}}^2$ denotes the PDR factor and the covariance $\sum_{r,t}^{\text{PDR}}$ in this factor is empirically set as the fixed value. $\|\mathbf{e}_{r,t}^M\|_{\Sigma_{r,t}^M}^2$ denotes the SMM factor. The covariance $\Sigma_{r,t}^M$ is empirically set as a fixed value in this factor.

7) *FGO-PDR-CV (4th Proposed Integration)*: The PDR and CV factors aided GNSS TC Doppler/pseudorange integration using FGO. The error function can be written as

$$\chi^* = \arg \min_{\chi} \sum_{s,t} \left(\|\mathbf{e}_{r,t}^D\|_{\Sigma_{r,t}^D}^2 + \|\mathbf{e}_{r,t}^s\|_{\Sigma_{r,t}^s}^2 + \|\mathbf{e}_{r,t}^R\|_{\sum_{r,t}^{\text{PDR}}}^2 + \|\mathbf{e}_{r,t}^C\|_{\Sigma_{r,t}^C}^2 \right) \quad (28)$$

FGO-PDR-CV is similar to FGO-PDR-SMM. The CV factor $\|\mathbf{e}_{r,t}^C\|_{\Sigma_{r,t}^C}^2$ is used for smoothing the trajectory, where $\Sigma_{r,t}^C$ is empirically set as a fixed value.

8) *FGO-PDR-CV-SMM (5th Proposed Integration)*: The PDR, CV, and SMM factors aided GNSS TC Doppler/pseudorange integration using FGO. The error function can be written as:

$$\chi^* = \arg \min_{\chi} \sum_{s,t} \left(\|\mathbf{e}_{r,t}^D\|_{\Sigma_{r,t}^D}^2 + \|\mathbf{e}_{r,t}^s\|_{\Sigma_{r,t}^s}^2 + \|\mathbf{e}_{r,t}^R\|_{\sum_{r,t}^{\text{PDR}}}^2 + \|\mathbf{e}_{r,t}^C\|_{\Sigma_{r,t}^C}^2 + \|\mathbf{e}_{r,t}^M\|_{\Sigma_{r,t}^M}^2 \right). \quad (29)$$

This method integrates all the proposed factors. Where $\|\mathbf{e}_{r,t}^D\|_{\Sigma_{r,t}^D}^2$ represents the TC Doppler frequency factor, detailed in Section III. The covariance $\Sigma_{r,t}^D$ is calculated using the satellite's C/N0 and ELE. Similarly, $\|\mathbf{e}_{r,t}^s\|$ is the pseudorange factor, also explained in Section III, with its covariance $\Sigma_{r,t}^s$ derived from the satellite C/N0 and ELE. The CV factor $\|\mathbf{e}_{r,t}^C\|_{\Sigma_{r,t}^C}^2$ is used for smoothing the trajectory, where $\Sigma_{r,t}^C$ is empirically set as a fixed value. $\|\mathbf{e}_{r,t}^R\|_{\sum_{r,t}^{\text{PDR}}}^2$ denotes the PDR factor and the covariance $\sum_{r,t}^{\text{PDR}}$ in this factor is empirically set as the fixed value. $\|\mathbf{e}_{r,t}^M\|_{\Sigma_{r,t}^M}^2$ denotes the SMM factor. The covariance $\Sigma_{r,t}^M$ is empirically set as a fixed value in this factor.

B. Derivation of the Double Difference Pseudorange Error

By comparing the true DD range with the DD pseudorange, we can get the quality of the used data. The raw pseudorange model can be expressed as

$$\rho_r^s = r_r^s + c(\delta_r - \delta_r^s) + I_r^s + T_r^s + \varepsilon_r^s \# \quad (30)$$

where r_r^s represents the actual range between the receiver r and the satellite s , δ_r is the receiver clock bias, δ_r^s is the satellite clock bias, I_r^s is the ionospheric delay, T_r^s is the tropospheric delay, ε_r^s is the system error, and c is the speed of light. For the user end and reference station r_1 and r_2 , we use $\rho_{r_1}^s$ and $\rho_{r_2}^s$ to represent the raw pseudorange measurements, respectively. By taking the difference between the pseudorange

of r_1 and r_2 , the double-differenced pseudorange is given by

$$\begin{aligned} \nabla \Delta \rho_{r_1, r_2}^{s,i} &= \nabla \rho_{r_1, r_2}^s - \nabla \rho_{r_1, r_2}^i \\ &= (r_{r_1}^s - r_{r_2}^s) - (r_{r_1}^i - r_{r_2}^i) + \varepsilon_{r_1, r_2}^{s,i} \end{aligned} \quad (31)$$

where $\varepsilon_{r_1, r_2}^{s,i}$ is the noise of the DD pseudorange. To evaluate the quality of the measurements, let \mathbf{p}^s be the position of satellite s , \mathbf{p}^i be the position of satellite i , \mathbf{p}_{r_1} be the position of receiver 1 from ground truth, and \mathbf{p}_{r_2} be the position of the reference station from the Rinex header position. \mathbf{p}^s , \mathbf{p}^i , \mathbf{p}_{r_1} , and \mathbf{p}_{r_2} are all defined in the ECEF frame. Then, the DD range $\nabla \Delta r_{r_1, r_2}^{s,i}$ can be written as

$$\begin{aligned} \nabla \Delta r_{r_1, r_2}^{s,i} &= (|\mathbf{p}^s - \mathbf{p}_{r_1}| - |\mathbf{p}^s - \mathbf{p}_{r_2}|) \\ &\quad - (|\mathbf{p}^i - \mathbf{p}_{r_1}| - |\mathbf{p}^i - \mathbf{p}_{r_2}|). \end{aligned} \quad (32)$$

Then, the DD pseudorange error can be expressed as

$$\nabla \Delta e_{r_1, r_2}^{s,i} = \nabla \Delta \rho_{r_1, r_2}^{s,i} - \nabla \Delta r_{r_1, r_2}^{s,i}. \quad (33)$$

REFERENCES

- [1] Y. Li et al., "Toward location-enabled IoT (LE-IoT): IoT positioning techniques, error sources, and error mitigation," *IEEE Internet Things J.*, vol. 8, no. 6, pp. 4035–4062, Mar. 2021, doi: [10.1109/JIOT.2020.3019199](https://doi.org/10.1109/JIOT.2020.3019199).
- [2] R. Sun et al., "Improving GPS code phase positioning accuracy in urban environments using machine learning," *IEEE Internet Things J.*, vol. 8, no. 8, pp. 7065–7078, Apr. 2021, doi: [10.1109/JIOT.2020.3037074](https://doi.org/10.1109/JIOT.2020.3037074).
- [3] P. D. Groves, "Principles of GNSS, inertial, and multisensor integrated navigation systems, [book review]," *IEEE Aerosp. Electron. Syst. Mag.*, vol. 30, no. 2, pp. 26–27, Feb. 2015.
- [4] P. D. Groves, Z. Jiang, M. Rudi, and P. Strode, "A portfolio approach to NLOS and multipath mitigation in dense urban areas," in *Proc. 26th Int. Techn. Meeting Satell. Divis. Inst. Navig.*, 2013, pp. 3231–3247.
- [5] L.-T. Hsu, Y. Gu, and S. Kamijo, "NLOS correction/exclusion for GNSS measurement using RAIM and city building models," *Sensors*, vol. 15, no. 7, pp. 17329–17349, 2015.
- [6] W. W. Wen, G. Zhang, and L.-T. Hsu, "GNSS NLOS exclusion based on dynamic object detection using LiDAR point cloud," *IEEE Trans. Intell. Transp. Syst.*, vol. 22, no. 2, pp. 853–862, Feb. 2021.
- [7] T. Suzuki and N. Kubo, "Correcting GNSS multipath errors using a 3D surface model and particle filter," in *Proc. 26th Int. Techn. Meeting Satell. Divis. Inst. Navig. (ION GNSS)*, 2013, pp. 1583–1595.
- [8] N. Sünderhauf and P. Protzel, "Towards robust graphical models for GNSS-based localization in urban environments," in *Proc. Int. Multi-Conf. Syst., Signals Devices*, 2012, pp. 1–6.
- [9] T. D. Barfoot, *State Estimation for Robotics*. Cambridge, U.K.: Cambridge Univ. Press, 2017.
- [10] W. Wen, T. Pfeifer, X. Bai, and L.-T. Hsu, "Factor graph optimization for GNSS/INS integration: A comparison with the extended Kalman filter," *Navig. J. Inst. Navig.*, vol. 68, no. 2, pp. 315–331, 2021.
- [11] T. Pfeifer and P. Protzel, "Expectation-maximization for adaptive mixture models in graph optimization," in *Proc. Int. Conf. Robot. Autom. (ICRA)*, 2019, pp. 3151–3157.
- [12] T. Pfeifer and P. Protzel, "Robust sensor fusion with self-tuning mixture models," in *Proc. IEEE/RSJ Int. Conf. Intell. Robots Syst. (IROS)*, 2018, pp. 3678–3685.
- [13] T. Pfeifer, S. Lange, and P. Protzel, "Dynamic covariance estimation—A parameter free approach to robust sensor fusion," in *Proc. IEEE Int. Conf. Multisens. Fusion Integr. Intell. Syst. (MFI)*, 2017, pp. 359–365.
- [14] T. Suzuki, "First place award winner of the smartphone decimeter challenge: Global optimization of position and velocity by factor graph optimization," in *Proc. 34th Int. Techn. Meeting Satell. Divis. Inst. Navig. (ION GNSS)*, 2021, pp. 2974–2985.
- [15] T. Suzuki, "1st place winner of the smartphone decimeter challenge: Two-step optimization of velocity and position using smartphone's carrier phase observations," in *Proc. 35th Int. Techn. Meeting Satell. Divis. Inst. Navig. (ION GNSS)*, 2022, pp. 2276–2286.

- [16] N. Sünderhauf and P. Protzel, "Switchable constraints for robust pose graph SLAM," in *Proc. IEEE/RSJ Int. Conf. Intell. Robots Syst.*, 2012, pp. 1879–1884.
- [17] W. Wen and L.-T. Hsu, "Towards robust GNSS positioning and Real-time kinematic using factor graph optimization," in *Proc. IEEE Int. Conf. Robot. Autom. (ICRA)*, 2021, pp. 5884–5890.
- [18] V. Capuano, L. Xu, and J. E. Benavides, "Smartphone MEMS accelerometer and gyroscope measurement errors: Laboratory testing and analysis of the effects on positioning performance," *Sensors*, vol. 23, no. 17, p. 7609, 2023.
- [19] R. Chen, W. Chen, X. Chen, X. Zhang, and Y. Chen, "Sensing strides using EMG signal for pedestrian navigation," *GPS Solut.*, vol. 15, pp. 161–170, Apr. 2011.
- [20] M. Basso, A. Martinelli, S. Morosi, and F. Sera, "A real-time GNSS/PDR navigation system for mobile devices," *Remote Sens.*, vol. 13, no. 8, p. 1567, 2021.
- [21] S. Beauregard and H. Haas, "Pedestrian dead reckoning: A basis for personal positioning," in *Proc. 3rd Workshop Position., Navig. Commun.*, 2006, pp. 27–35.
- [22] U. Steinhoff and B. Schiele, "Dead reckoning from the pocket—an experimental study," in *Proc. IEEE Int. Conf. Pervasive Comput. Commun. (PerCom)*, 2010, pp. 162–170.
- [23] Q. Wang et al., "Pedestrian dead reckoning based on walking pattern recognition and online magnetic fingerprint trajectory calibration," *IEEE Internet Things J.*, vol. 8, no. 3, pp. 2011–2026, Feb. 2021, doi: [10.1109/JIOT.2020.3016146](https://doi.org/10.1109/JIOT.2020.3016146).
- [24] D. Yan, C. Shi, T. Li, and Y. Li, "FlexPDR: Fully flexible pedestrian dead reckoning using online multimode recognition and time-series decomposition," *IEEE Internet Things J.*, vol. 9, no. 16, pp. 15240–15254, Aug. 2022, doi: [10.1109/JIOT.2022.3147473](https://doi.org/10.1109/JIOT.2022.3147473).
- [25] C. Chen, P. Zhao, C. X. Lu, W. Wang, A. Markham, and N. Trigoni, "Deep-learning-based pedestrian inertial navigation: Methods, data set, and on-device inference," *IEEE Internet Things J.*, vol. 7, no. 5, pp. 4431–4441, May 2020, doi: [10.1109/JIOT.2020.2966773](https://doi.org/10.1109/JIOT.2020.2966773).
- [26] W. Chen, R. Chen, Y. Chen, H. Kuusniemi, and J. Wang, "An effective pedestrian dead reckoning algorithm using a unified heading error model," in *Proc. IEEE/ION Position, Locat. Navig. Symp.*, 2010, pp. 340–347, doi: [10.1109/PLANS.2010.5507300](https://doi.org/10.1109/PLANS.2010.5507300).
- [27] W. Kang and Y. Han, "SmartPDR: Smartphone-based pedestrian dead reckoning for indoor localization," *IEEE Sensors J.*, vol. 15, no. 5, pp. 2906–2916, May 2015.
- [28] J. Kuang, X. Niu, and X. Chen, "Robust pedestrian dead reckoning based on MEMS-IMU for smartphones," *Sensors*, vol. 18, no. 5, p. 1391, 2018.
- [29] S. Y. Cho and C. G. Park, "Threshold-less zero-velocity detection algorithm for pedestrian dead reckoning," in *Proc. Eur. Navig. Conf. (ENC)*, 2019, pp. 1–5.
- [30] F. Zhu, X. Tao, W. Liu, X. Shi, F. Wang, and X. Zhang, "Walker: Continuous and precise navigation by fusing GNSS and MEMS in smartphone chipsets for pedestrians," *Remote Sens.*, vol. 11, no. 2, p. 139, 2019.
- [31] J. Ye, Y. Li, H. Luo, J. Wang, W. Chen, and Q. Zhang, "Hybrid urban canyon pedestrian navigation scheme combined PDR, GNSS and beacon based on smartphone," *Remote Sens.*, vol. 11, no. 18, p. 2174, 2019.
- [32] R. Harle, "A survey of indoor inertial positioning systems for pedestrians," *IEEE Commun. Surveys Tuts.*, vol. 15, no. 3, pp. 1281–1293, 3rd Quart., 2013.
- [33] C. Wei et al., "An integrated GPS and multi-sensor pedestrian positioning system for 3D urban navigation," in *Proc. Joint Urban Remote Sens. Event*, 2009, pp. 1–6, doi: [10.1109/URS.2009.5137690](https://doi.org/10.1109/URS.2009.5137690).
- [34] A. Rehman, H. Shahid, M. A. Afzal, and H. M. A. Bhatti, "Accurate and direct GNSS/PDR integration using extended Kalman filter for pedestrian smartphone navigation," *Gyroscopy Navig.*, vol. 11, no. 2, pp. 124–137, 2020, doi: [10.1134/S2075108720020054](https://doi.org/10.1134/S2075108720020054).
- [35] C. Jiang et al., "Smartphone PDR/GNSS integration via factor graph optimization for pedestrian navigation," *IEEE Trans. Instrum. Meas.*, vol. 71, pp. 1–12, Jun. 2022, doi: [10.1109/TIM.2022.3186082](https://doi.org/10.1109/TIM.2022.3186082).
- [36] A. Angrisano, M. Vultaggio, S. Gaglione, and N. Crocetto, "Pedestrian localization with PDR supplemented by GNSS," in *Proc. Eur. Navig. Conf. (ENC)*, 2019, pp. 1–6.
- [37] L.-T. Hsu, Y. Gu, Y. Huang, and S. Kamijo, "Urban pedestrian navigation using smartphone-based dead reckoning and 3-D map-aided GNSS," *IEEE Sensors J.*, vol. 16, no. 5, pp. 1281–1293, Mar. 2016.
- [38] L. Wang, P. D. Groves, and M. K. Ziebart, "Smartphone shadow matching for better cross-street GNSS positioning in urban environments," *J. Navig.*, vol. 68, no. 3, pp. 411–433, 2015.
- [39] S. Malkos, "Google to provide raw GNSS measurements: User location takes center stage in new android OS," *GPS World*, vol. 27, no. 7, p. 36, 2016.
- [40] Y. Zhong, W. Wen, H.-F. Ng, X. Bai, and L.-T. Hsu, "Real-time factor graph optimization aided by graduated non-convexity based outlier mitigation for smartphone decimeter challenge," in *Proc. 35th Int. Techn. Meeting Satell. Divis. Inst. Navig. (ION GNSS)*, 2022, pp. 2339–2348.
- [41] W. Wen, G. Zhang, and L.-T. Hsu, "GNSS outlier mitigation via graduated non-convexity factor graph optimization," *IEEE Trans. Veh. Technol.*, vol. 71, no. 1, pp. 297–310, Jan. 2022.
- [42] A. M. Herrera, H. F. Suhandri, E. Realini, M. Reguzzoni, and M. C. de Lacy, "goGPS: Open-source MATLAB software," *Gps Solut.*, vol. 20, no. 3, pp. 595–603, 2016.
- [43] T. Takasu and A. Yasuda, "Development of the low-cost RTK-GPS receiver with an open source program package RTKLIB," in *Proc. Int. Symp. GPS/GNSS*, 2009, pp. 1–6.
- [44] H. Weinberg, "Using the ADXL202 in pedometer and personal navigation applications," *Analog Devices AN-602 Appl. Note*, vol. 2, no. 2, pp. 1–6, 2002.
- [45] D. Kamisaka, S. Muramatsu, T. Iwamoto, and H. Yokoyama, "Design and implementation of pedestrian dead reckoning system on a mobile phone," *IEICE Trans. Inf. Syst.*, vol. 94, no. 6, pp. 1137–1146, 2011.
- [46] H.-F. Ng, G. Zhang, and L.-T. Hsu, "A computation effective range-based 3D mapping aided GNSS with NLOS correction method," *J. Navig.*, vol. 73, no. 6, pp. 1202–1222, 2020.
- [47] S. P. Drake, *Converting GPS Coordinates [Phi, Lambda, h] to Navigation Coordinates (ENU)*, Defense Techn. Inf. Center Gov. Dept., Fort Belvoir, VA, USA, 2002.
- [48] S. Agarwal and K. Mierle, "Ceres solver," 2012. [Online]. Available: <http://ceres-solver.org/>
- [49] J. J. Moré, "The Levenberg-Marquardt algorithm: implementation and theory," in *Proc. Numer. Anal. Biennial Conf. Held Dundee*, 1978, pp. 105–116.
- [50] J. Ortiz, M. Pupilli, S. Leutenegger, and A. J. Davison, "Bundle adjustment on a graph processor," in *Proc. IEEE/CVF Conf. Comput. Vis. Pattern Recognit.*, 2020, pp. 2416–2425.
- [51] T. Wübbena, F. Darugna, A. Ito, and J. Wübbena, "Geo++'s Experiments on android GNSS raw data," in *Proc. GNSS Raw Meas. Taskforce Workshop, GSA Hqrs.*, 2018.
- [52] S. Malkos, "User location takes center stage in new android OS: Google to provide raw GNSS measurements," *GPS World*, vol. 27, no. 7, p. 36, 2016.
- [53] L.-T. Hsu et al., "Hong Kong UrbanNav: An open-source multisensory dataset for benchmarking urban navigation algorithms," *Navig. J. Inst. Navig.*, vol. 70, no. 4, pp. 1–29, 2023.
- [54] F. Huang, W. Wen, J. Zhang, and L.-T. Hsu, "Point wise or feature wise? A benchmark comparison of publicly available LiDAR odometry algorithms in urban canyons," *IEEE Intell. Transp. Syst. Mag.*, vol. 14, no. 6, pp. 155–173, Nov./Dec. 2022.
- [55] L. Zhang, H.-F. Ng, G. Zhang, and L.-T. Hsu, "3D mapping aided GNSS positioning using doppler frequency for urban areas," in *Proc. 36th Int. Techn. Meeting Satell. Divis. Inst. Navig. (ION GNSS)*, 2023, pp. 2897–2905.
- [56] T. Shan, B. Englot, D. Meyers, W. Wang, C. Ratti, and D. Rus, "LIO-SAM: Tightly-coupled Lidar inertial odometry via smoothing and mapping," in *Proc. IEEE/RSJ Int. Conf. Intell. Robots Syst. (IROS)*, 2020, pp. 5135–5142.
- [57] W. Wen, T. Pfeifer, X. Bai, and L.-T. Hsu, "It is time for factor graph optimization for GNSS/INS integration: Comparison between FGO and EKF," 2020, [arXiv:2004.10572](https://arxiv.org/abs/2004.10572).
- [58] "Web download of SatRef GNSS raw data (RINEX Format)," Accessed: Nov. 27, 2023. [Online]. Available: <https://www.geodetic.gov.hk/en/rinex/downvn.aspx>
- [59] R. J. Lisle, "Google earth: A new geological resource," *Geol. today*, vol. 22, no. 1, pp. 29–32, 2006.
- [60] M. Haklay and P. Weber, "OpenStreetMap: User-generated street maps," *IEEE Pervasive Comput.*, vol. 7, no. 4, pp. 12–18, Oct.–Dec. 2008.
- [61] P. Xie and M. G. Petovello, "Measuring GNSS multipath distributions in urban canyon environments," *IEEE Trans. Instrum. Meas.*, vol. 64, no. 2, pp. 366–377, Feb. 2015.
- [62] W. Wen, X. Bai, and L.-T. Hsu, "3D vision aided GNSS real-time kinematic positioning for autonomous systems in urban canyons," *Navigat. J. Inst. Navig.*, vol. 70, no. 3, pp. 1–39, 2023.



Yihan Zhong received the bachelor's degree in process equipment and control engineering from Guangxi University, Nanning, China, in 2020, and the master's degree from The Hong Kong Polytechnic University, Hong Kong, in 2022, where he is currently pursuing the Ph.D. degree with the Department of Aeronautical and Aviation Engineering.

His research interests include factor graph optimization-based collaborative positioning and low-cost localization.



Li-Ta Hsu received the B.S. and Ph.D. degrees in aeronautics and astronautics from National Cheng Kung University, Tainan, Taiwan, in 2007 and 2013, respectively.

He is currently an Associate Professor with the Department of Aeronautical and Aviation Engineering, The Hong Kong Polytechnic University, Hong Kong. He served as a Postdoctoral Researcher with the Institute of Industrial Science, University of Tokyo, Tokyo, Japan. In 2012, he was a Visiting Scholar with University College London, London, U.K. His research interests include GNSS positioning in challenging environments and localization for pedestrians, autonomous driving vehicle, and unmanned aerial vehicle.



Weisong Wen (Member, IEEE) received the B.Eng. degree in mechanical engineering from Beijing Information Science and Technology University, Beijing, China, in 2015, the M.Eng. degree in mechanical engineering from China Agricultural University, Beijing, in 2017, and the Ph.D. degree in mechanical engineering from The Hong Kong Polytechnic University (PolyU), Hong Kong, in 2020.

He was also a visiting Ph.D. student with the Faculty of Engineering, University of California at Berkeley, Berkeley, CA, USA, in 2018. Before joining with PolyU as an Assistant Professor in 2023, he has been a Research Assistant Professor with the Department of Aeronautical and Aviation Engineering, PolyU since 2021. He has published 30 SCI papers and 40 conference papers in the field of GNSS (ION GNSS+) and navigation for Robotic systems (IEEE ICRA and IEEE ITSC), such as autonomous driving vehicles.

Dr. Wen won the Innovation Award from the TechConnect in 2021, the Best Presentation Award from the Institute of Navigation in 2020, and the First Prize in Hong Kong Section in Qianhai-Guangdong-Macao Youth Innovation and Entrepreneurship Competition in 2019 based on his research achievements in 3D LiDAR aided GNSS positioning for robotics navigation in urban canyons. The developed 3D LiDAR-aided GNSS positioning method has been reported by top magazines, such as Inside GNSS and has attracted industry recognition with remarkable knowledge transfer.